ELSEVIER

International Journal of Heat and Fluid Flow 21 (2000) 49–57

International Journal of
HEAT AND
FLUID FLOW

www.elsevier.com/locate/ijhff

Relaminarization of turbulent flow in the entrance region of a rapidly rotating channel

G.K. Dutzler [1], B.A. Pettersson-Reif [2], H.I. Andersson *

Division of Applied Mechanics, Faculty of Mechanical Engineering, The Norwegian University of Science and Technology, N-7491 Trondheim, Norway

Received 24 August 1997; accepted 23 September 1999

Abstract

Second-moment closure predictions of developing turbulent flow in a plane channel subjected to rapid spanwise rotation are compared with experimental results. Near-wall effects are modelled by elliptic relaxation. Rapid pressure–strain interactions are accounted for by a non-linear, cubic model which employs variable coefficients and is consistent with the principle of material frame indifference (MFI) in the limit of two-dimensional turbulence. It is shown that the rotational-induced effect of the Coriolis force on the developing mean flow field and the turbulence quantities is well reproduced by the present approach. It is particularly encouraging that the experimentally observed relaminarization on the stabilized suction side of the channel could be predicted well.

Keywords: Turbulent channel flow; Elliptic relaxation; System rotation; Second-moment closure

Notation

a_{ij}	Reynolds stress anisotropy, $\overline{u_iu_j}/k - 2\delta_{ij}/3$
A_2	second Reynolds stress invariant, $a_{ij}a_{ij}$
A_3	third Reynolds stress invariant, $a_{ik}a_{kj}a_{ji}$
$d^{\rm p}_{ij}$	pressure diffusion of $\overline{u_iu_j}$
$d^{\rm t}_{ij}$	turbulent diffusion of $\overline{u_iu_j}$
$d^{\rm v}_{ij}$	viscous diffusion of $\overline{u_iu_j}$
f_{ij}	intermediate variable
F	flatness parameter, $1 - 9(A_2 - A_3)/8$
H	channel half-width
k	turbulent kinetic energy, $\overline{u_iu_j}/2$
L	turbulent length scale
P	mean static pressure
P^*	reduced mean static pressure, $P^* = P - \rho\Omega^2 x_i x_i/2$
P_k	production rate of turbulent kinetic energy, $P_{ii}/2$
P_{ij}	production rate of $\overline{u_iu_j}$ due to mean shear
R_{ij}	production rate of $\overline{u_iu_j}$ due to system rotation
Re	global Reynolds number, $Re = U_{\rm m}H/\nu$
Ro	rotation number, $Ro = 2\Omega H/U_{\rm m}$
S_{ij}	mean rate-of-strain tensor, $(\partial_j U_i + \partial_i U_j)/2$
T	turbulent time scale
U_i	mean velocity in x_i-direction
$U_{\rm c}$	centreline velocity
$U_{\rm m}$	bulk mean velocity
U^+	streamwise mean velocity normalized by wall friction velocity, U_1/u_τ
u_i	x_i-component of fluctuating velocity
u'	root mean square value of u
u_τ	wall friction velocity, $\sqrt{\tau_{\rm W}/\rho}$
$-\overline{u_iu_j}$	kinematic Reynolds stress
W_{ij}	mean intrinsic vorticity tensor, $(\partial_j U_i - \partial_i U_j)/2 + \epsilon_{jik}\Omega_k$
x, y, z	Cartesian coordinates defined in Fig. 1
y^+	inner variable, yu_τ/ν
ϵ_{ijk}	permutation tensor
$\wp_{ij}$	relaxed pressure–strain tensor

Greeks

δ_{ij}	Kronecker delta
ε	energy dissipation rate, $\varepsilon_{ii}/2$
ε_{ij}	dissipation rate tensor
μ	dynamic viscosity
ν	kinematic viscosity
ρ	density
$\tau_{\rm w}$	wall shear stress, $\mu\partial U/\partial y\|_{\rm w}$
Φ	mean viscous dissipation function
Φ_{ij}	pressure–strain interactions
Ω	angular velocity defined in Fig. 1

Superscripts

h	homogeneous part
p	pressure part
t	turbulent part
r	rapid part

---

* Corresponding author.
E-mail address: helge.i.andersson@mtf.ntnu.no (H.I. Andersson).

[1] Present address: BMW Motoren GmbH, A-4400 Steyr, Austria.

[2] Present address: Kongsberg Defence & Aerospace, N-3601 Kongsberg, Norway.

0142-727X/00/$ - see front matter
PII: S0142-727X(99)00069-7

v	viscous part
$+$	wall coordinates
$'$	root mean square value

Subscripts

c	centreline
m	bulk mean
w	wall value
1,2	value of streamwise and wall-normal components

1. Introduction

Fluid flow in non-inertial frames of reference are encountered in a variety of engineering applications. Among these are for instance the flow through a radial compressor impeller or the internal flow in cooling passages of gas turbine bladings. The Coriolis force associated with imposed system rotation is known to profoundly affect, not only the mean flow field, but also the intensity and structure of the turbulence. There exists considerable interest to accurately predict these effects since the performance of an actual machine component can be degraded significantly at off-design conditions.

Computational fluid dynamics (CFD) has become an essential design tool in many industries. For most engineering applications in the foreseeable future, this approach will be based on Reynolds-averaged Navier–Stokes equations (RANS). The success of a CFD analysis inevitably depends strongly on the adopted turbulence model. It is therefore unfortunate that the most frequently adopted models are based on Boussinesq's linear eddy-viscosity hypothesis, e.g. the k–ε model. An inherent shortcoming of these closures is their frame indifference property. In other words, they are insensitive to the imposed system rotation.

To extend the predictive capability of linear eddy-viscosity closures, non-linear models have been proposed in the literature (e.g. Speziale, 1987). In these, non-linear elements of the mean deformation rate tensors are retained in the constitutive equation. System rotation enters the stress–strain relationship explicitly through the mean intrinsic vorticity tensor. However, in these models the relation for the shear stress reduces to the commonly used linear form in the limit of parallel shear flow (the non-linear terms are zero). This is true for all constant-coefficient, non-linear eddy-viscosity models that are realizable, cf. Speziale (1998). Parallel shear flow, although superficially simple, constitutes an important basic flow relevant to numerous engineering applications.

Second-moment closures (SMCs) are the most natural closure level for computing flows affected by body forces due to e.g. imposed system rotation or streamline curvature. In contrast to scalar-based models, e.g. k–ε, the individual components of the Reynolds stress tensor are obtained from a set of modelled transport equations. The potential advantage of SMCs is due to the natural appearance of exact production terms due to mean shear and system rotation. The convective transport of second moments is also retained in its exact form.

A viable and less computational expensive alternative would be to adopt a so-called explicit algebraic stress model (EASM). An EASM can formally be derived from elaborate SMCs and it constitutes an exact solution of the SMC in the limit of homogeneous and equilibrium turbulence (cf. Pope 1975; Gatski and Speziale 1993). In this limit, production terms due to mean shear and system rotation from the SMC transport equations can be retained in their exact form. Its constitutive relation has the same generic form as a non-linear eddy-viscosity model but the coefficients are functions of dimensionless velocity-gradient parameters rather than being constants. Although these closures are promising, they are ambiguous; their form depends on the coordinate system in which they are derived. Furthermore, EASMs are formally only valid in homogeneous, equilibrium turbulence which rarely is encountered in flows of engineering interest.

The majority of engineering flows are characterized by non-equilibrium, near-wall turbulence. Within the framework of SMCs, the important a priori unknown, pressure–strain correlation tensor is traditionally modelled by invoking a quasi-equilibrium assumption. However, this model usually needs to be modified in the proximity of e.g solid boundaries. Durbin (1993) introduced the so-called elliptic relaxation approach to incorporate near-wall effects into SMCs. It differs from the traditional wall-echo terms introduced into earlier models as additive corrections (cf. e.g. Launder et al., 1975). Instead of an ad hoc wall damping term, elliptic near-wall effects are introduced by solving a Helmholtz equation with the quasi-homogeneous pressure–strain model as source term. Since the formulation is independent of source representation, any quasi-homogeneous pressure–strain model can be used. No wall topography parameters are used, so the method is directly applicable to general geometries. It has successfully been applied to a variety of flows, not only in inertial frames (Durbin, 1993; Pettersson-Reif and Andersson, 1999), but also in non-inertial systems (Wizman et al., 1996; Pettersson and Andersson, 1997).

Numerous experimental studies of *fully developed* channel flow subjected to spanwise rotation have been performed. Among the earlier ones are e.g. Launder (1965), Moore (1967) and Johnston et al. (1972). Through improved computing resources, highly accurate direct numerical simulations (DNS) have become feasible, however, this approach is still limited to relatively low Reynolds numbers. Kristoffersen and Andersson (1993) reported DNS results of fully developed channel flow subject to spanwise rotation. A salient feature of this particular flow is that the effect of the imposed rotation on the mean flow field enters *only* via the turbulence equations. It constitutes therefore a good benchmark test for the assessment of turbulence closures in rotating frames of reference, see e.g. Launder and Tselepidakis (1994) and Pettersson and Andersson (1997). The impact of the Coriolis force depends not only on the magnitude, but also on the orientation of the rotation vector. Depending on the sense of rotation, augmentation and reduction of the turbulent intensity is expected on the corresponding pressure and suction side of the channel, respectively. The imposed rotation not only breaks the symmetry of the mean flow field, it may eventually also lead to relaminarization. The reduced turbulence level implies less mean momentum transfer towards the surface whereby e.g. in a general geometry the tendency for flow separation to occur is increased.

However, in the majority of engineering applications, the flow field cannot be considered fully developed. Instead, *developing* boundary layers are more common. The objective of the present investigation is therefore to assess the performance of a near-wall SMC for the developing flow in the entrance region of a *rapidly* rotating plane channel. The experimental measurements reported by Koyama and Ohuchi (1985) are used as reference data. This is an especially challenging test case since the flow tends to relaminarize on one side of the channel and the near-wall modelling therefore plays a crucial role. The elliptic relaxation approach is adopted in conjunction with the pressure–strain model due to Ristorcelli et al. (1995). The low-Re approach is strongly motivated by the fact that reliable computations of complex wall-flows require a proper representation of wall boundary conditions. This cannot in general be achieved by the wall-function approach. The present SMC fulfils the principle of material frame indifference (MFI) in the limit of two-dimensional turbulence, which makes the choice suitable for rapidly rotating flows. The present study is a sequel to our recent investigation (Dutzler et al., 1997), in which a developing channel flow subjected to moderate spanwise rotation was considered.

2. The mathematical model

2.1. Mean flow equations

The problem under consideration is that of incompressible and developing turbulent channel flow shown schematically in Fig. 1. The steady mean flow is in the xy-plane and the channel is rotated with constant angular velocity Ω about the z-axis. The governing Reynolds-averaged equations for mass continuity and momentum can be written in Cartesian tensor notation as:

$$\frac{\partial U_i}{\partial x_i} = 0, \tag{1}$$

$$\rho \frac{\partial}{\partial x_j}(U_i U_j) = -\frac{\partial P^*}{\partial x_i} + \frac{\partial}{\partial x_j}\left(\mu \frac{\partial U_i}{\partial x_j} - \rho \overline{u_i u_j}\right) - 2\rho \Omega_j U_k \epsilon_{ijk}, \tag{2}$$

where U_i and u_i denote mean and fluctuating parts of the velocity component in the x_i-direction, respectively. $P^* = P - (1/2)\rho\Omega^2(x^2 + y^2)$ denotes the reduced mean static pressure and P is the mean pressure.

2.2. Turbulence modelling

The unknown Reynolds stresses $-\rho\overline{u_i u_j}$ in Eq. (2) can be obtained from the exact Reynolds stress transport equation which can be written as:

$$\frac{D\,\overline{u_i u_j}}{Dt} = P_{ij} + R_{ij} + d^{\mathrm{v}}_{ij} + d^{\mathrm{t}}_{ij} + d^{\mathrm{p}}_{ij} + \wp_{ij} - \frac{\overline{u_i u_j}}{k}\varepsilon, \tag{3}$$

where

$$P_{ij} = -\left(\overline{u_{\mathrm{m}} u_i}\frac{\partial U_j}{\partial x_{\mathrm{m}}} + \overline{u_{\mathrm{m}} u_j}\frac{\partial U_i}{\partial x_{\mathrm{m}}}\right), \tag{4a}$$

$$R_{ij} = -2\Omega_k\left(\overline{u_{\mathrm{m}} u_i}\epsilon_{jk\mathrm{m}} + \overline{u_{\mathrm{m}} u_j}\epsilon_{ik\mathrm{m}}\right), \tag{4b}$$

$$d^{\mathrm{v}}_{ij} = \nu \frac{\partial^2 \overline{u_i u_j}}{\partial x_k \partial x_k}, \tag{4c}$$

$$d^{\mathrm{t}}_{ij} + d^{\mathrm{p}}_{ij} = -\frac{\partial}{\partial x_k}\left(\overline{u_i u_j u_k}\right) - \frac{1}{\rho}\frac{\partial}{\partial x_k}\left(\overline{p u_i}\delta_{jk} + \overline{p u_j}\delta_{ik}\right), \tag{4d}$$

$$\wp_{ij} = \underbrace{\overline{\frac{p}{\rho}\left(\frac{\partial u_i}{\partial x_j} + \frac{\partial u_j}{\partial x_i}\right)}}_{\Phi_{ij}} - \varepsilon_{ij} + \frac{\overline{u_i u_j}}{k}\varepsilon \tag{4e}$$

are the production due to mean shear P_{ij} and system rotation R_{ij}, viscous, turbulent and pressure diffusion d^{v}_{ij}, d^{t}_{ij}, d^{p}_{ij} and the 'relaxed' pressure–strain tensor $\wp_{ij}$. The last term in Eq. (3) is Rotta's anisotropic model for the dissipation rate tensor ε_{ij}.

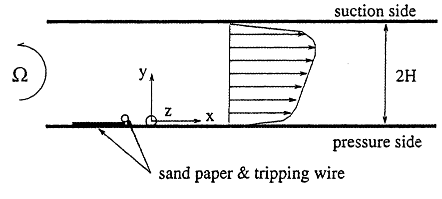

Fig. 1. Schematic of flow configuration and coordinate system.

δ_{ij} is the Kronecker delta and ϵ_{ijk} denotes the permutation tensor. $\nu = \mu/\rho$ is the kinematic viscosity. For steady mean flow the local change in $\overline{u_i u_j}$ is zero and the convective terms become the only contributions to the substantial derivative $D\overline{u_i u_j}/Dt$. The important generation terms P_{ij} and R_{ij} need no modelling and enter the $\overline{u_i u_j}$ equations in their exact form. The primary effect of system rotation can therefore be incorporated in a natural way. In addition, rotational terms enter the modelled rapid pressure–strain correlation through the mean intrinsic vorticity. The viscous diffusion term d^{v}_{ij} can also be retained in its exact form whereas the unclosed diffusion terms d^{t}_{ij} and d^{p}_{ij} in Eq. (4d) are modelled together by gradient diffusion as

$$d^{\mathrm{t}}_{ij} + d^{\mathrm{p}}_{ij} = \frac{\partial}{\partial x_{\mathrm{n}}}\left(C_{\mathrm{K}}\overline{u_{\mathrm{n}} u_{\mathrm{m}}} T \frac{\partial \overline{u_i u_j}}{\partial x_{\mathrm{m}}}\right), \tag{5}$$

where T is a turbulent time scale, cf. Eq. (9).

Durbin's elliptic relaxation equation: The redistribution tensor $\wp_{ij}$ in Eq. (4e) is obtained from the solution f_{ij} of the elliptic relaxation equation proposed by Durbin (1993), which can be put into coordinate-independent form and written as follows:

$$\wp_{ij} = k f_{ij}, \tag{6a}$$

$$L^2 \nabla^2 f_{ij} - f_{ij} = -\frac{\wp^{\mathrm{h}}_{ij}}{k}, \tag{6b}$$

$\wp^{\mathrm{h}}_{ij}$ denotes the quasi-homogeneous form of $\wp_{ij}$, f_{ij} is an intermediate variable and L is a turbulent length scale usually taken as

$$L = C_{\mathrm{L}} \max\left(\frac{k^{3/2}}{\varepsilon}, C_\eta\left(\frac{\nu}{\varepsilon}\right)^{1/4}\right) \tag{7}$$

with the Kolmogorov length scale as a lower bound.

The elliptic relaxation equation (6b) is a modified Helmholtz equation and accounts indirectly for non-local effects within the flow, which are caused by the proximity of a solid boundary. These effects are kinematic blocking of the wall-normal velocity fluctuation and pressure reflections from the surface. This approach is attractive since Eqs. (6a) and (6b) is free of wall distances and unit vectors which make the model applicable to flows bounded by a complex geometry. Through imposed boundary conditions on Eq. (6b), non-homogeneous effects of a wall can be represented. Far from the surface the effect of the elliptic operator in Eq. (6b), vanishes and $\wp_{ij}$ relaxes to its quasi-homogeneous form $\wp^{\mathrm{h}}_{ij} = k f_{ij}$. Furthermore, far from the wall locally isotropic dissipation can be assumed, i.e. $\varepsilon_{ij} = 2\delta_{ij}\varepsilon/3$, and Eq. (4e) reduces to $\wp^{\mathrm{h}}_{ij} = \Phi^{\mathrm{h}}_{ij} + a_{ij}\varepsilon$, where $a_{ij} = \overline{u_i u_j}/k - 2\delta_{ij}/3$ is the Reynolds stress anisotropy tensor. Any quasi-homogeneous pressure–strain model can be used in place of Φ^{h}_{ij}. This study adopts the non-linear model due to Ristorcelli et al. (1995) hereafter denoted as RLA, see Appendix A. The right-hand side of Eq. (6b) then takes the form

$$\frac{\wp^{\mathrm{h}}_{ij}}{k} = \frac{\Phi^{\mathrm{hr}}_{ij}}{k} + \frac{(1 - C_1)}{T}a_{ij}, \tag{8}$$

where T is a turbulent time scale defined as

$$T = \max\left(\frac{k}{\varepsilon}, 6.0\left(\frac{\nu}{\varepsilon}\right)^{1/2}\right) \tag{9}$$

with Kolmogorovs time scale as a lower bound, in analogy with Eq. (7). The purpose of introducing the Kolmogorov scale in Eq. (9) is to avoid a singularity in Eq. (10) as $k \to 0$ at a solid boundary.

Table 1
Model constants

$C_{\varepsilon 1}$	$C_{\varepsilon 2}$	C_{K}	C_{ε}	C_{L}	C_{η}
1.44	1.85	0.19	0.14	0.18	647

In order to close the set of governing equations, the dissipation rate ε of the turbulent kinetic energy k is obtained from its own modelled transport equation:

$$\frac{\partial}{\partial x_j}\left(U_j\varepsilon\right) = \frac{C_{\varepsilon 1}^{*}P_k - C_{\varepsilon 2}\varepsilon}{T} + \frac{\partial}{\partial x_j}\left(\nu\frac{\partial\varepsilon}{\partial x_j} + C_{\varepsilon}T\overline{u_iu_j}\frac{\partial\varepsilon}{\partial x_i}\right), \tag{10}$$

where $C_{\varepsilon 1}^{*} = C_{\varepsilon 1}(1 + 0.1(P_k/\varepsilon))$ and the use of the time scale T are the only modifications of the standard high-*Re* model equation.

The model equation governing the turbulent kinetic energy is given by

$$\frac{\partial}{\partial x_j}\left(U_jk\right) = P_k - \varepsilon + \frac{\partial}{\partial x_j}\left(\nu\frac{\partial k}{\partial x_j} + C_{\mathrm{K}}T\overline{u_iu_j}\frac{\partial k}{\partial x_i}\right). \tag{11}$$

The present study adopts a somewhat modified form of the turbulent lenght scale L in conjunction with the RLA pressure–strain model. This modification is related to an observation of Wizman et al. (1996) who found that in the logarithmic-layer the original formulation of the elliptic relaxation equation (Durbin, 1993) tends to amplify the redistribution of energy among the components of the Reynolds stress tensor, in opposition to what is expected. In order to embed the correct wall-echo effect Wizman et al. (1996) reformulated the elliptic relaxation model and proposed a so-called neutral formulation. Instead of altering the elliptic relaxation equation, Pettersson and Andersson (1997) proposed to modify the length scale L: the coefficients (C_{L} and C_{η}) in Eq. (7) are replaced by

$$\tilde{C}_{\mathrm{L}} = C_{\mathrm{L}}A_2^{1/2}, \quad \tilde{C}_{\eta} = C_{\eta}A_2^{-1/2}\exp\left(-\left(\frac{1 + A_3}{0.1 + A_2}\right)^2\right), \tag{12}$$

respectively, where $A_2 = a_{ij}a_{ji}$ denotes the second and $A_3 = a_{ik}a_{kj}a_{ji}$ the third Reynolds-stress invariants. Model constants are listed in Table 1.

The flow in a rotating channel can relaminarize due to the stabilizing effect of the Coriolis force. This gives rise to a singularity in Eq. (7) as $\varepsilon \to 0$. In order to remove this singularity, Pettersson and Andersson (1997) replaced the dissipation rate ε in Kolmogorov's length scale by $\hat{\varepsilon} = \sqrt{\varepsilon^2 + \Phi^2}$, where Φ is the mean viscous dissipation function defined as $2\nu S_{kl}S_{kl}$ and S_{kl} denotes the mean rate-of-strain tensor. The length scale in Eq. (6b) now takes the final form

$$L = \tilde{C}_{\mathrm{L}}\max\left(\frac{k^{3/2}}{\varepsilon}, \tilde{C}_{\eta}\left(\frac{\nu^3}{\hat{\varepsilon}}\right)^{1/4}\right). \tag{13}$$

3. Numerical method

The present study uses a modified version of the elliptic finite-volume solver TEAM-RSM (Huang and Leschziner, 1983). The code solves for 11 variables stored in a staggered grid arrangement. The spanwise stress component $\overline{u_3^2}$ is not solved for but instead derived from the relation $\overline{u_3^2} = 2k - \overline{u_1^2} - \overline{u_2^2}$, where $\overline{u_1^2}(\equiv \overline{u^2})$ is the streamwise and $\overline{u_2^2}(\equiv \overline{v^2})$ the wall-normal stress component. In the mean momentum equations the convection terms are approximated by the Quadratic Upstream-weighted Interpolation scheme (QUICK) while in the equations for k, ε and $\overline{u_iu_j}$ the Power-Law-Differencing Scheme (PLDS) is used. The SIMPLE algorithm is used to handle the important velocity–pressure linkage. The transport equations for the Reynolds-stresses are solved simultaneously with their corresponding f_{ij}-equations ($\overline{u_iu_j} - f_{ij}$ systems) and the k–ε equations are solved as a coupled pair. The resulting set of algebraic equations is solved semi-implicitely by a tridiagonal matrix algorithm for the momentum equations and by a block-tridiagonal matrix algorithm for the k–ε and $\overline{u_iu_j} - f_{ij}$ systems using alternating sweep directions. The coupling between the pairs of equations is dictated primarily by a coupling in the boundary conditions. Solving two equations at a time results in a more stable scheme.

To further enhance the stability of the second-moment computations a fully staggered arrangement of all stress locations relative to mean-velocity locations is used. This practice results in a stronger coupling between the stresses and the associated driving mean strains (Huang and Leschziner, 1985). Furthermore, the stress transport equations are recast into a form permitting a part of each stress to be expressed as a gradient-type diffusion, like $\nu_{ij}\partial U_i/\partial x_j$, and a remaining residual stress. Here, ν_{ij} is an unconditional positive apparent viscosity. The residual stresses are included into the source terms whereas the gradient-type diffusion is included into the diffusion terms of the mean momentum equations in order to enhance the numerical stability. In addition, it is discriminated between positive contributions to the source which are added to the uniform part of the source term and negative ones which are included into the proportional part of the source term (Huang and Leschziner, 1985).

No-slip boundary conditions were used at the solid walls together with $k = \partial k/\partial y = 0$ for the k–ε system and $\overline{u_iu_j} = 0$ and

$$f_{ij} = \begin{cases} -\frac{20\nu^2}{\varepsilon_{\mathrm{w}}y_1^4}\left(\overline{u_iu_j}\right)_1 & i \text{ and/or } j \text{ in wall-normal direction,} \\ 0 & i \text{ and } j \text{ in tangential direction,} \end{cases}$$

where $\varepsilon_{\mathrm{w}} = 2\nu k_1/y_1^2$. Subscript 1 denotes the wall adjacent computational node. The boundary conditions for f_{ij} can be derived from the local solution of the model equation governing the wall-normal stress component $\overline{u_2^2}$ at the wall (cf. Durbin, 1993). Inflow and outflow boundary conditions are discussed in the next section. The calculations were carried out on a 100×50 (cross-stream × streamwise) Cartesian grid system. The first grid point in the cross-stream direction was located at about $y^+ \approx 0.5$ and moderate grid expansion was applied towards the channel centre. In the streamwise direction a highly expanded grid was generated so that a large portion of grid points was used to cover the experimentally investigated area of developing flow in the entrance region of the channel. This grid layout was found to be sufficient to obtain a grid-independent solution. The solution was considered to be numerically converged when the sum of absolute normalized residuals over the calculation domain fell below 10^{-4}.

4. Numerical results and discussion

Extensive results from experimental investigations of developing two-dimensional boundary layers in a rotating wind tunnel have been published by Koyama et al. (1979) and Koyama and Ohuchi (1985). The straight test channel had cross-sectional dimensions of 280 mm × 40 mm (z- and y-directions) and a length of 670 mm (x-direction, see Fig. 1). With this aspect ratio of 7:1, two-dimensional boundary layers accompanied by a potential core were found to exist in the centre-region of the channel. The free stream turbulence in the potential core was about 2%. A hot-wire system was used to measure the mean velocity and the streamwise turbulence intensity at six different downstream locations. The first profile at $x = 0$ was obtained 55 mm downstream the inlet and the streamwise spacing between the measuring stations was 100 mm.

The present computations were carried out for two different cases with the bulk mean velocity $U_{\mathrm{m}} = 5$ m/s and an angular velocity of $\Omega = 0$ rad/s and $\Omega = 10\pi$ rad/s (i.e. 300 rpm), respectively. The global Reynolds number $Re = U_{\mathrm{m}}H/\nu$ based on the channel half-width H (cf. Fig. 1), was approximately 5900. The rotation number, defined as $Ro = 2H\Omega/U_{\mathrm{m}}$ was either zero or 0.25. The rectangular calculation domain was 2000 mm long, i.e. four times longer than the distance from the first to the last measuring station, thus ensuring fully developed flow conditions at the outlet of the calculation domain.

Care was taken to ensure fully consistent inlet conditions for the numerical computations since the available set of experimental data was insufficient to provide profiles for all dependent variables. In the experiments, the developing boundary layers were unfortunately tripped on one side only. A sand paper and a tripping wire were mounted on the wall at $y = 0$ just upstream of the inlet to the test section (see Fig. 1). Therefore, the flow remained laminar under certain conditions on the opposite side ($y = 2H$). When calculations were based on measured inflow conditions, convergence was possible only for the case when the channel was rotated such that the turbulence level was enhanced on the *untripped* side, i.e. for $\Omega < 0$. To circumvent this difficulty the following approach was adopted: In the non-rotating case the data on the tripped side of the channel were assigned to both sides, thereby resulting in a symmetric profile across the channel. In the rotating case, on the other hand, the asymmetric inlet velocity profile was derived by matching two turbulent mean velocity profiles for $\Omega > 0$ and $\Omega < 0$ taken from the *tripped* channel side: The profile from $y = 0$ to $y = H$ for $\Omega < 0$ was mirrored on the channel centre line from $y = H$ to $y = 2H$ and matched with the velocity profile from $y = 0$ to $y = H$ for $\Omega > 0$. By means of this approach, fully turbulent cross-sectional profiles were achieved. Exactly the same procedure was used to generate the inlet profile for the streamwise turbulence intensity $\overline{u^2}$. By this approach inlet boundary conditions were prescribed in accordance with the measured distributions of U and $\overline{u^2}$ at the first measurement station (cf. Nilsen and Andersson, 1994). For all other quantities, reasonable approximations were necessary and the following procedure was used: Calculations were first performed for fully developed flow conditions with $Re = 5900$ and $Ro = 0$. From the converged solution, profiles from the wall to the centreline for $\overline{v^2}$ and $\overline{w^2}$ were adjusted to the actual boundary layer thickness. This was also done for the shear stress $\overline{uv}$, the f_{ij}-values and the dissipation rate ε. In the potential core, isotropic turbulence was assumed. Furthermore, the magnitudes of the $\overline{v^2}$ and $\overline{w^2}$ inside the boundary layers were adjusted such that the ratio $\overline{u^2}$:$\overline{v^2}$:$\overline{w^2}$ were the same as in the solution for the fully developed flow case. Subsequently, the profile for the turbulent kinetic energy was computed from its definition $k = \overline{u_iu_i}/2$ and the wall values of ε and f_{ij} were adjusted according to the boundary conditions given in Section 3. The Schwarz inequality, which for this case reads $(\overline{uv})^2 \leqslant \overline{u^2} \cdot \overline{v^2}$, was not violated by this procedure. A linear cross-stream pressure distribution adjusted to the rotation rate was prescribed. This is in accordance to the quasi-one-dimensional potential flow analysis of Rothe and Johnston (1976). Through this procedure, a fully consistent set of input data was derived.

Computed profiles of mean velocity U and streamwise turbulence intensity $u' = (\overline{u^2})^{1/2}$ for the non-rotating case at three different streamwise positions are presented in Figs. 2 and 3, respectively. The predictions are compared with the experimental findings of Koyama and Ohuchi (1985). As can be seen from the results, the boundary layer thickness increases while the potential core shrinks as the flow develops downstream. According to the predictions, the boundary layers merge at about $x = 500$ mm and, eventually, fully developed flow conditions are established further downstream of $x = 1500$ mm. This observation suggests first that the imposed fully developed flow boundary conditions at the outlet can be justified and secondly that the flow at the final measuring station ($x = 500$ mm) is far from being fully developed. However, the actual growth of the boundary layers is somewhat overpredicted. The reason for this may be attributed to the two-dimensional assumption of the calculation whereby the displacement effect of the end-wall boundary layers at $z = 0$ and $z = 280$ mm is not accounted for. According to the experiments, the boundary layers would merge slightly downstream of $x = 500$ mm. The peak of the streamwise turbulence intensity shown in Fig. 3 is captured quite well by the model except at $x = 300$ mm where it is somewhat underpredicted. This can partly be explained by the fact that u' has been normalized by the computed centre line velocity U_{c} which is too high as compared to the experiments due to the overestimated boundary layer growth. The overall agreement is, however, satisfactory.

Figs. 4 and 5 display the streamwise turbulence intensity and the mean velocity distributions for $Re = 5900$ and $Ro = 0.25$. In our preceding investigation of the same flow configuration (Dutzler et al., 1997), $Re = 11\,800$ and $Ro = 0.12$. Nakabayashi and Kitoh (1996) suggested that the combination $Ro/(2\,Re)$ is the essential parameter in wall-bounded flows subject to system rotation. They used the

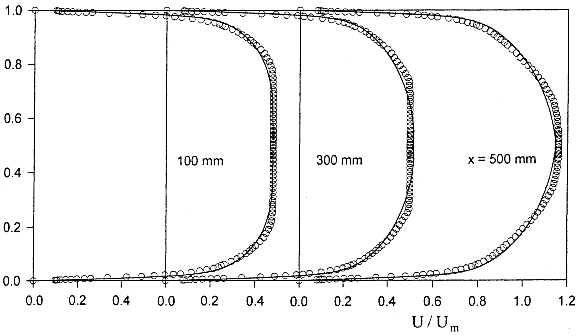

Fig. 2. Profiles of streamwise distribution of mean velocity U at three different locations for $Ro = 0$; computed results (lines) are compared with experimental data (symbols) of Koyama and Ohuchi (1985).

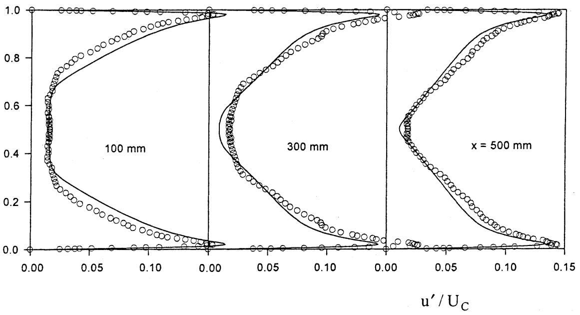

Fig. 3. Profiles of streamwise turbulence intensity u' at three different locations for $Ro = 0$ (legend as in Fig. 2).

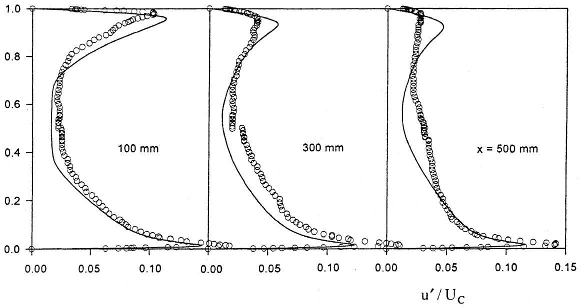

Fig. 4. Profiles of streamwise turbulence intensity *u*' at three different locations for $Ro = 0.25$ (legend as in Fig. 2).

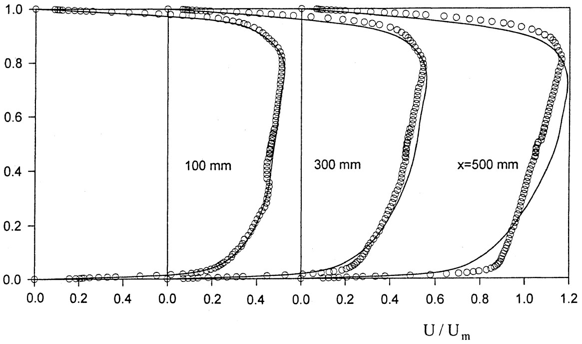

Fig. 5. Profiles of streamwise distribution of mean velocity U at three different locations for $Ro = 0.25$ (legend as in Fig. 2).

friction velocity as the velocity scale in their analysis, while the bulk mean velocity is adopted in the present study. Thus, the paramenter $Ro/(2\ Re) = \Omega\nu/U_{\mathrm{m}}^2$ has been increased by a factor 4 in the present study as compared to our previous calculations (Dutzler et al., 1997), thereby suggesting a much stronger influence of rotation on the overall structure of the turbulent flow field. Indeed, Fig. 4 displays a substantial reduction of the streamwise turbulence intensity on the stabilized suction side of the channel. The highly asymmetric mean velocity profiles in Fig. 5 exhibit the characteristic shift of the maximum velocity towards the suction side of the channel. The overall agreement between the mean velocity profiles and the measurements are good. At the final measuring station ($x = 500$ mm), however, some deviations occur on the unstable side ($y/2H = 0$). These can be ascribed to the experimentally observed Taylor–Görtler (TG) like vortices in the y–z plane which can not be captured by a two-dimensional calculation in the x–y plane, cf. Fig. 1. The experiments also show a nearly linear velocity distribution in the channel centre with almost zero absolute mean vorticity, i.e. $\partial U/\partial y \approx 2\Omega$. The slope of the computed velocity profiles in the irrotational potential core is in good agreement with the experiments, but this region becomes somewhat narrower due to the overpredicted boundary layer growth.

The predictions of the streamwise turbulence intensity in Fig. 4 along the leading pressure side ($y/2H = 0$) indicate an underestimation of the peak in the vicinity of the wall and in the centre of the channel while in the log-layer up to $y^+ \approx 150$ they coincide quite well with the experimental data. This discrepancy can again be explained by the existence of TG-like vortices, as conjectured earlier by Nilsen and Andersson (1994). The rotational-induced reduction of the streamwise turbulence intensity at the trailing suction side ($y/2H = 1.0$) is somewhat underpredicted by the model, but the overall reduction is substantially more pronounced than in our earlier calculations (Dutzler et al., 1997). The measurements at the stabilized suction side exhibit a reduction of the peak level to the free stream turbulence level, which thereby suggests that relaminarization occurs, see also Koyama and Ohuchi (1985).

In fact, Fig. 6 displays the predicted shear stress distribution at the downstream position $x = 500$ mm, where the model returned a substantial region of *almost* zero shear stress which expands over about 50% of the channel width. This indicates a complete relaminarization at the stabilized suction side of the channel. Furthermore, Fig. 6 clearly demonstrates that the present modelling approach is capable of predicting this flow phenomenon.

The different boundary layer development along the two walls is obviously associated with the difference in the turbulence levels near the suction and pressure side, respectively. Examinations of how system rotation affects the turbulent flow field are frequently based on an analysis of the exact production terms due to mean shear P_{ij} and system rotation R_{ij} in the otherwise modelled transport equations for the individual Reynolds stress components, see Eqs. (3)–(4b). The rotational production $R_{22} = -4\Omega\overline{uv}$ tends to increase (reduce) the wall-normal stress component at the pressure (suction) channel side. Since $R_{11} = -R_{22}$, opposite effects of rotation might be expected on the streamwise component $\overline{u^2}$. However, one has to consider the total production $P_{11} + R_{11}$ of the streamwise component. For the fully developed flow case, which is a reasonable approximation for the present situation, we obtain:

$$P_{11} + R_{11} = -2\overline{uv}\frac{\partial U}{\partial y} + 4\Omega\overline{uv} = P_{11}\left(1 - \frac{2\Omega}{\partial U/\partial y}\right). \qquad (14)$$

For moderately weak rotation, i.e. $|2\Omega/(\partial U/\partial y)| \ll 1$, Eq. (14) is dominated by the changes in the mean shear producion P_{11}, which is indirectly affected by system rotation through the Coriolis effect on $\overline{v^2}$. This is so because the wall-normal turbulence intensity enters the primary shear production $P_{12} = -\overline{v^2}\partial U/\partial y$ which directly affects the shear stress distribution and in turn enters Eq. (14) via $\overline{uv}$. For higher rotation rates, $\overline{v^2}$ exceeds $\overline{u^2}$ on the pressure side and the rotational production $R_{12} = 2\Omega(\overline{u^2} - \overline{v^2})$ tends to reduce the magnitude of $\overline{uv}$ and in turn the total production $P_{11} + R_{11}$ of $\overline{u^2}$. In fact, Fig. 7 shows the variation of $\overline{v^2}/\overline{u^2}$ across the channel. A reversal of the conventional ratio between $\overline{v^2}$ and $\overline{u^2}$ (i.e. $\overline{v^2}/\overline{u^2} < 1$) occurs over a substantial part of the channel which

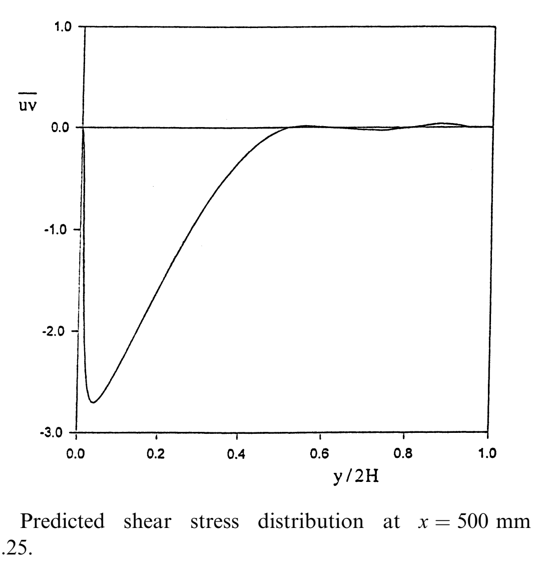

Fig. 6. Predicted shear stress distribution at $x = 500$ mm for $Ro = 0.25$.

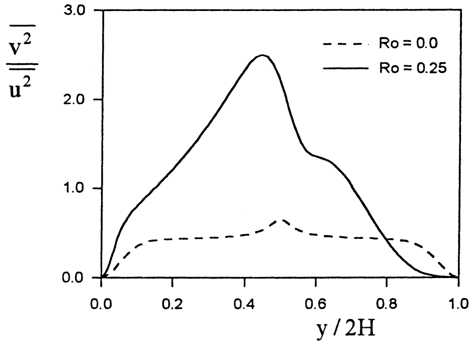

Fig. 7. Predicted variation of $\overline{v^2}/\overline{u^2}$ at $x = 500$ mm.

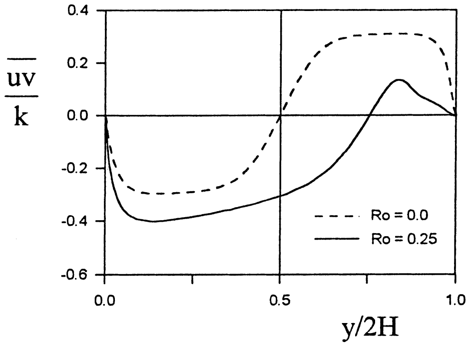

Fig. 9. Predicted variation of the structural parameter $\overline{uv}/k$ at the outlet $x = 2000$ mm.

penetrates far into the pressure side boundary layer. This explains the gradual reduction of the peak of the streamwise turbulence intensity (Fig. 4) at the pressure side as the flow develops downstream. It is indeed encouraging that the rotational-induced reduction of the streamwise intensity along the pressure side is reproduced by the model predictions. The notion of the pressure side as the destabilized side of a rotating channel can therefore be misleading.

Fig. 8 shows the predicted variation of P/ε at the outlet where fully developed flow conditions are established. The model predicts local equilibrium turbulence only on the pressure side of the rotating channel where the production approximately equals the dissipation rate. On the suction side, however, a substantial deviation can be observed. These findings are in agreement with the DNS results of Andersson and Kristoffersen (1995) who concluded that the wall-function approach based on the assumption $P \approx \varepsilon$ should be abandoned in rotating turbulent flows. Moreover, a small region of negative turbulent energy production, i.e. $P < 0$, near the channel centre can also be observed which also is consistent with the DNS results (Andersson and Kristoffersen, 1995). In this region, mean flow energy is extracted from the turbulence. Since negative turbulent production arises from opposite signs of the mean velocity gradient and the turbulent shear stress, this phenomenon cannot be predicted by models based on the eddy-viscosity hypothesis.

The variation of the structural parameter $\overline{uv}/k$ at the channel outlet ($x = 2$ m) is shown in Fig. 9. In the rotating flow case the profile exhibits a substantial deviation from the common value 0.3 in the log-layer which is implicitly assumed in the wall-function approach.

Fig. 10 shows the predicted mean velocity profile in wall units for the non-rotating and rotating cases at the downstream position $x = 0.5$ m. For the non-rotating case the model predictions exhibit a logarithmic profile in close agreement with the 'law-of-the-wall'. For the rotating case, on the other hand, it is evident that the wake component is enhanced on the suction side of the channel whereas on the pressure side, it is completely eliminated. The profiles on the suction side show a typical laminar-like shape. The deviation from the logarithmic distribution increases as the rotation number is raised.

Finally, Fig. 11 shows the predicted streamwise development of the friction velocity $u_\tau = (|\tau_w|/\rho)^{1/2}$ for the non-rotating (dashed line) and rotating flow case $Ro = 0.25$ (lines) and comparisons are made with the Preston-tube measurements (symbols) of Koyama and Ohuchi (1985). The significant effect of rotation on the wall friction is captured well on the suction side. However, the monotonic increase on the pressure side could not be reproduced by the model. The reason for this may be attributed to the assumption of two-dimensionality in the computations, an assumption which is also questionable in the experiments. Obviously, two counteracting effects are present along the pressure side: the thickening of the boundary layer tends to reduce the wall friction, whereas the enhanced turbulent agitation due to the Coriolis force and the TG like vortices tend to increase the wall friction. The data in Fig. 11 suggest that the latter effect is the more prominent in the experimental setup. It should also be noted that there is a minor anomaly in the experimental

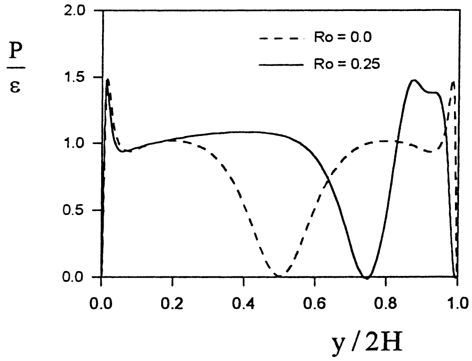

Fig. 8. Predicted variation of P/ε at the outlet $x = 2000$ mm.

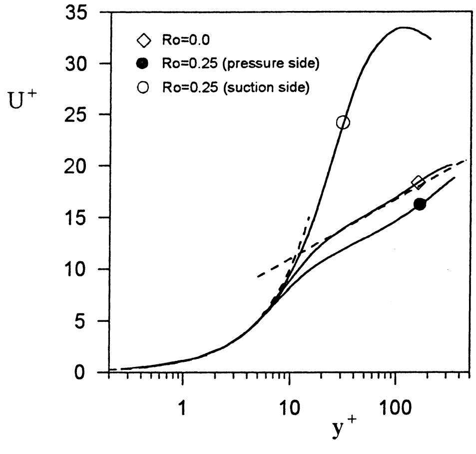

Fig. 10. Mean velocity distributions in wall units for $Ro = 0$ and $Ro = 0.25$ at $x = 500$ mm (symbols are used to reference the lines to their corresponding rotation number).

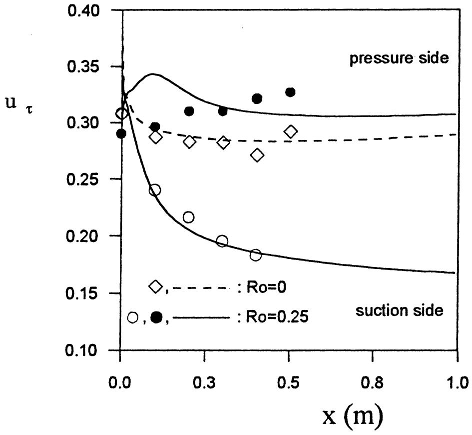

Fig. 11. Streamwise development of the friction velocity for $Ro = 0$ and $Ro = 0.25$.

results, namely that the friction velocity on the suction side is initially *larger* than on the pressure side.

5. Concluding remarks

An elaborate near-wall Reynolds stress model has been used to compute the boundary layer development in a rapidly rotating plane channel. To account for the rapid pressure–strain interactions, the non-linear variable-coefficient model due to Ristorcelli et al. (1995) was employed. The novel elliptic relaxation approach was used to model near-wall effects. The overall agreement with the experimental findings of Koyama and Ohuchi (1985) is good, although the boundary layer growth is somewhat overpredicted. This may be attributed to the two-dimensional assumption of the flow in the calculations which may be only partly valid in the laboratory channel. On the unstable pressure side, minor deviations occur which are ascribed to the experimentally observed, rotationally induced, longitudinal TG like vortices. To further investigate these issues, fully three-dimensional computations are required so that the blockage effect of the end-wall boundary layers and the rotationally induced vortical roll cells can be resolved. However, the model is able to reproduce the experimentally observed relaminarization on the stabilized suction side of the channel. These achievements are ascribed to the novel near-wall treatment introduced by Durbin (1993). A substantial reduction of the streamwise turbulence intensity and an almost zero turbulent shear stress over a large portion on the stabilized side of the channel was observed. Furthermore, the computational results indicated that the turbulence field is far from being in equilibrium on the stabilized suction side and that a tiny region of negative production of turbulence energy exists in the channel core. This is fully consistent with the DNS results reported by Andersson and Kristoffersen (1995) for fully developed channel flow.

Acknowledgements

The authors are grateful to Professor H.S. Koyama at the Tokyo Denki University for generously making the experimental data available. The constructive criticism of the reviewers, together with the advice of Professor B.E. Launder, helped us in the preparation of a better focused paper.

Appendix A. Pressure–strain correlation

A.1. The Ristorcelli, Lumley and Abid (RLA) model

Ristorcelli et al. (1995) proposed a non-linear model for the *rapid* pressure–strain correlation Φ_{ij}^{hr} which involves cubic terms in the anisotropy tensor $b_{ij} = a_{ij}/2$ and employs variable-coefficients which are functions of the Reynolds stress invariants. The RLA model statisfies a weak form of realizability which ensures positive normal Reynolds stress components.

The *geostrophic constraint* implies that in the limit of rapid rotation the portion of the rapid pressure–strain correlation associated with rotation must balance the Coriolis terms R_{ij} in the modelled second-moment equations, therefore, leaving the equations independent of rotation. This led to another rigorous form of realizability which the RLA model fulfils: the principle of MFI in the limit of two-dimensional turbulence, see also Speziale (1998). This is a direct consequence of the Taylor–Proudman theorem which requires that the equations must be independent of rotation when the velocity field is two-dimensionalized in a plane perpendicular to the axis of rotation. The general form of the model for the rapid pressure–strain is

$$\begin{aligned}\frac{\Phi_{ij}^{\mathrm{hr}}}{4k} &= \left(C_3 - 2\mathrm{II}C_3'' + 3\mathrm{III}C_3'''\right)S_{ij} + C_4\left(b_{ik}S_{kj} + b_{jk}S_{ik} - \frac{2}{3}b_{kl}S_{kl}\delta_{ij}\right)\\ &\quad + C_4'''b_{kl}S_{kl}\left(b_{ij}^2 + \frac{2}{3}\delta_{ij}\mathrm{II}\right) + C_5\left(b_{ik}W_{kj} + b_{jk}W_{ki}\right)\\ &\quad + b_{ij}\left(C_6 b_{kl}S_{kl} + C_4''' b_{lk}b_{k\mathrm{m}}S_{l\mathrm{m}}\right)\\ &\quad + C_7\left(b_{ik}^2 S_{kj} + b_{jk}^2 S_{ki} - \frac{2}{3}\delta_{ij}b_{lk}b_{k\mathrm{m}}S_{l\mathrm{m}}\right)\\ &\quad + C_8\left(b_{ik}^2 W_{kj} + b_{jk}^2 W_{ki}\right) + C_9\left(b_{ik}W_{lk}b_{lj}^2 + b_{jk}W_{lk}b_{li}^2\right), \qquad (\mathrm{A.1})\end{aligned}$$

where

$$S_{ij} = \frac{1}{2}\left(\frac{\partial U_i}{\partial x_j} + \frac{\partial U_j}{\partial x_i}\right), \quad W_{ij} = \frac{1}{2}\left(\frac{\partial U_i}{\partial x_j} - \frac{\partial U_j}{\partial x_i}\right) + \epsilon_{jik}\Omega_k \qquad (\mathrm{A.2})$$

are the mean rate-of-strain tensor and the mean intrinsic vorticity tensor and $b_{ij}^2 = b_{ik}b_{kj}$. $\mathrm{II} = -b_{ij}b_{ij} = -A_2/8$ and $\mathrm{III} = b_{ik}b_{kj}b_{ji}/3 = A_3/24$ are the second and third Reynolds stress invariants, respectively. The variable coefficients of Eq. (A.1) are given in Ristorcelli et al. (1995).

For the slow pressure–strain Φ_{ij}^{hs} a simple linear Rotta-type model of the form $\Phi_{ij}^{\mathrm{hs}} = -C_1\varepsilon(\overline{u_i u_j} - (2/3)k\delta_{ij})/k = -C_1\varepsilon a_{ij}$ is used in Eq. (8). However, for the variable linear-return coefficient, the expression $C_1 = (2 - 31\mathrm{II}F^{1/2})/2$ was invented by Ristorcelli et al. (1995) where $F = 1 - (9/8)(A_2 - A_3)$ is the flatness parameter.

References

Andersson, H.I., Kristoffersen, R., 1995. Turbulence statistics of rotating channel flow. Turbulent Shear Flows, vol. 9. Springer, Berlin, pp. 53–70.

Durbin, P.A., 1993. A Reynolds stress model for near-wall turbulence. J. Fluid Mech. 249, 465–498.

Dutzler, G.K., Pettersson, B.A., Andersson, H.I., 1997. Modelling aspects of developing turbulent channel flow in orthogonal mode rotation. In: Proceedings of the 10th International Conference on Numerical Methods in Laminar and Turbulent Flow. Pineridge Press, Swansea, pp. 393–404.

Gatski, T.B., Speziale, C.G., 1993. On explicit algebraic stress models for complex turbulent flows. J. Fluid Mech. 249, 59–78.

Huang, P.G., Leschziner, M.A., 1983. An introduction and guide to the computer code TEAM. UMIST Mech. Eng. Dept. Rep. TFD/83/9/R.

Huang, P.G., Leschziner, M.A., 1985. Stabilization of recirculating-flow computations performed with second-moment closures and third-order discretization. In: Proceedings of the Fifth Symposium on Turbulent Shear Flows. Ithaca, New York, pp. 20.7–20.12.

Johnston, J.P., Halleen, R.M., Lezius, D., 1972. Effects of spanwise rotation on the structure of two-dimensional fully developed turbulent channel flow. J. Fluid Mech. 56, 533–557.

Koyama, H., Masuda, S., Ariga, I., Watanabe, I., 1979. Stabilizing and destabilizing effects of Coriolis force on two-dimensional laminar and turbulent boundary layers. ASME J. Eng. Power 101, 23–31.

Koyama, H.S., Ohuchi, M., 1985. Effects of Coriolis force on boundary layer development. In: Proceedings of the Fifth Symposium on Turbulent Shear Flows. Ithaca, New York, pp. 21.19–21.24.

Kristoffersen, R., Andersson, H.I., 1993. Direct numerical simulations of low Reynolds number turbulent flow in a rotating channel. J. Fluid Mech. 256, 163–197.

Launder, B.E., 1965. The effect of Coriolis force on fully-developed flow in a rotating duct. MIT Gas Turb. Lab. Rep.

Launder, B.E., Reece, G., Rodi, W., 1975. Progress in the development of a Reynolds-stress turbulence closure. J. Fluid Mech. 68, 537–566.

Launder, B.E., Tselepidakis, D.P., 1994. Application of a new second-moment closure to turbulent channel flow rotating in orthogonal mode. Int. J. Heat Fluid Flow 15, 2–10.

Moore, J., 1967. Effects of Coriolis force on turbulent flow in rotating rectangular channels. MIT Gas Turb. Lab. Rep. 89.

Nakabayashi, K., Kitoh, O., 1996. Low Reynolds number fully developed two-dimensional turbulent channel flow with system rotation. J. Fluid Mech. 315, 1–29.

Nilsen, P.J., Andersson, H.I., 1994. Developing turbulent flow in a rotating channel. Int. J. Heat Fluid Flow 15, 100–103.

Pettersson, B.A., Andersson, H.I., 1997. Near-wall Reynolds-stress modelling in noninertial frames of reference. Fluid Dyn. Res. 19, 251–276.

Pettersson-Reif, B.A., Andersson, H.I., 1999. Second-moment closure predictions of turbulence-induced secondary flow in a straight square duct. Engineering Turbulence Modelling and Experiments, vol. 4. Elsevier, pp. 349–358.

Pope, S.B., 1975. A more general eddy-viscosity hypothesis. J. Fluid Mech. 72, 331–340.

Ristorcelli, J.R., Lumley, J.L., Abid, R., 1995. A rapid-pressure covariance representation consistent with the Taylor–Proudman theorem materially frame indifferent in the two-dimensional limit. J. Fluid Mech. 292, 111–152.

Rothe, P.H., Johnston, J.P., 1976. Effects of system rotation on the performance of two-dimensional diffusers. ASME J. Fluids Eng., 422–430.

Speziale, C.G., 1987. On nonlinear K–l and K–ε models of turbulence. J. Fluid Mech. 178, 459–475.

Speziale, C.G., 1998. A consistency condition for non-linear algebraic Reynolds stress models in turbulence. Int. J. Non-linear Mech. 33, 579–584.

Wizman, V., Laurence, D., Kanniche, M., Durbin, P.A., Demuren, A., 1996. Modeling near-wall effects in second-moment closures by elliptic relaxation. Int. J. Heat Fluid Flow 17, 255–266.